NANO LETTERS

Letter

pubs.acs.org/NanoLett

# Optical Torques on Upconverting Particles for Intracellular Microrheometry

Paloma Rodríguez-Sevilla,[†] Yuhai Zhang,[‡] Nuno de Sousa,[§,∥] Manuel I. Marqués,[⊥] Francisco Sanz-Rodríguez,[†,#] Daniel Jaque,[*,†,#] Xiaogang Liu,[‡] and Patricia Haro-González[†]

[†]Fluorescence Imaging Group, Departamento de Física de Materiales, Universidad Autónoma de Madrid, 28049 Madrid, Spain

[‡]Department of Chemistry, National University of Singapore, Science Drive 3, Singapore 117543, Singapore

[§]Departamento de Física de la Materia Condensada, Condensed Matter Physics Center (IFIMAC), and Nicolás Cabrera Institute, Universidad Autónoma de Madrid, 28049 Madrid, Spain

[∥]Donostia International Physics Center (DIPC), Donostia-San Sebastián 20018, Spain

[⊥]Departamento de Física de Materiales, Condensed Matter Physics Center (IFIMAC), and Nicolás Cabrera Institute, Universidad Autónoma de Madrid, 28049 Madrid, Spain

[#]Instituto Ramón y Cajal de Investigaciones Sanitarias, Hospital Ramón y Cajal, Madrid 28034, Spain

Supporting Information

**ABSTRACT:** Precise knowledge and control over the orientation of individual upconverting particles is extremely important for full exploiting their capabilities as multifunctional bioprobes for interdisciplinary applications. In this work, we report on how time-resolved, single particle polarized spectroscopy can be used to determine the orientation dynamics of a single upconverting particle when entering into an optical trap. Experimental results have unequivocally evidenced the existence of a unique stable configuration. Numerical simulations and simple numerical calculations have demonstrated that the dipole magnetic interactions between the upconverting particle and trapping radiation are the main mechanisms responsible of the optical torques that drive the upconverting particle to its stable orientation. Finally, how a proper analysis of the rotation dynamics of a single upconverting particle within an optical trap can provide valuable information about the properties of the medium in which it is suspended is demonstrated. A proof of concept is given in which the laser driven intracellular rotation of upconverting particles is used to successfully determine the intracellular dynamic viscosity by a passive and an active method.

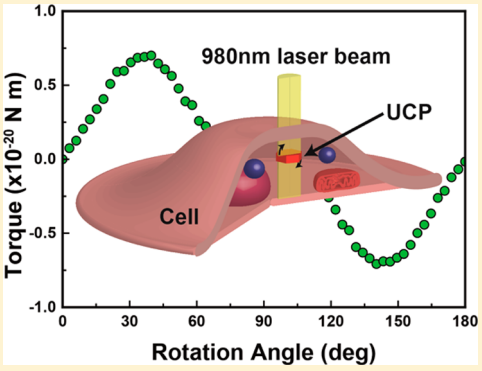


**KEYWORDS:** *Optical trapping, upconverting particle, optical torque, finite element method, viscosity, microrheometry*

The possibility of achieving three-dimensional (3D) control over nano/micro objects by optical trapping (OT) has boosted the development of new remote manipulation techniques that have widened frontiers of many research fields.[1−3] Early development of OT was motivated by the fact that optical forces (in the order of pN) were comparable to those exerted on organelles inside cells.[4,5] OT early consolidated as a very useful technique for biological investigations allowing, for example, the study of the mechanical properties of fundamental biological components such as proteins or DNA chains or remote particle manipulation during endoscopy procedures.[2,6−8] OT allows for the remote manipulation of a wide variety of probes such as biological elements, entire cells, or nonorganic particles made of different materials (metallic, dielectric, and so forth).[9−19] In particular, OT of single upconverting particles (UCPs) has recently attracted great interest as it constitutes a new window for the development of minimally invasive thermal characterization techniques. As an example, OT of a single UCP is at the basis of the acquisition of 3D thermal maps in the surroundings of living cells and plasmonic structures with submicrometric resolution.[20] In these cases, thermal scanning was performed by the real time analysis of the thermosensitive two-photon luminescence generated by a single optically trapped UCP. Such analysis is simple and straightforward for spherical (isotropic) UCPs because their emission spectrum does not depend on the orientation of the UCP inside the optical trap. On the contrary, nonspherical UCPs show highly polarized emission spectra and therefore their luminescence would be strongly determined by their particular orientation inside the trap.[21,22] This makes essential the knowledge of the particular orientation of single UCPs inside an optical trap as well as the understanding of the physical mechanism leading to this orientation.

**Received:** November 2, 2016
**Published:** November 14, 2016





DOI: 10.1021/acs.nanolett.6b04583
*Nano Lett.* 2016, 16, 8005−8014

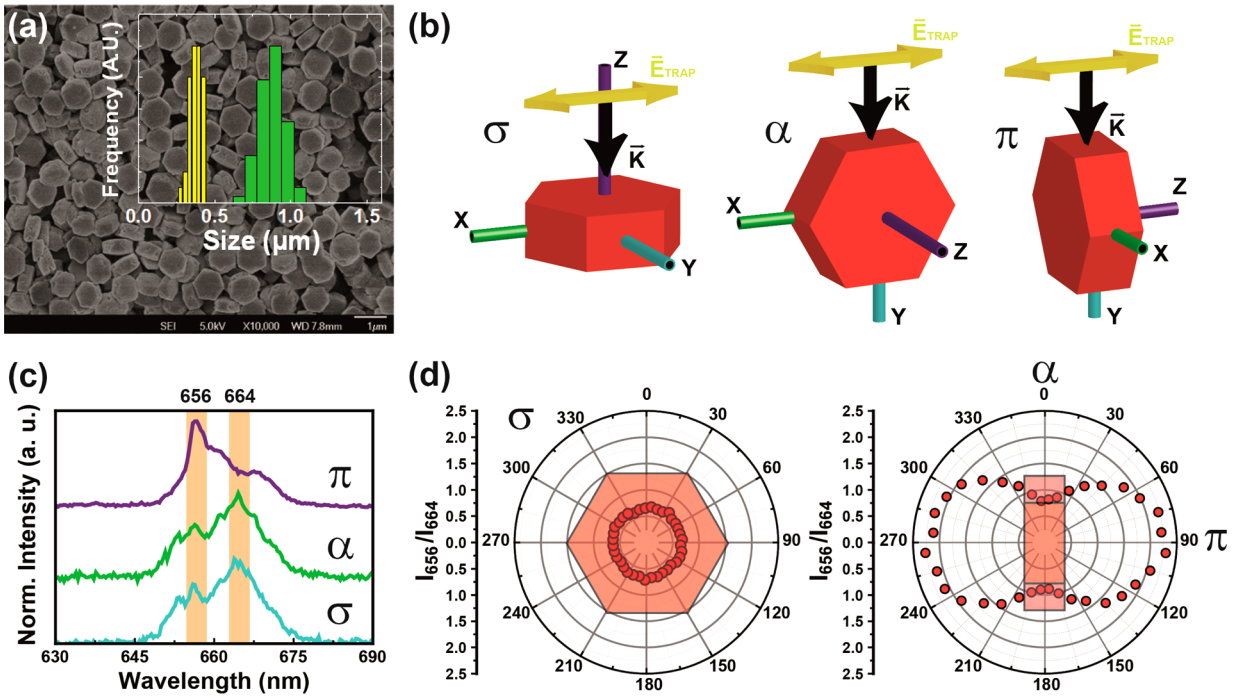


**Figure 1.** (a) Surface electron microscopy image of the $NaYF_4$:$Er^{3+}$,$Yb^{3+}$ particles with thickness and diameter histograms (yellow and green, respectively). (b) Diagrams of the three excitation configurations. In $\sigma$-polarization, light propagates along the optical axis ($z$-axis) with a polarization perpendicular to it. In $\alpha$- and $\pi$-polarizations light propagates perpendicularly to the crystal axis with a polarization perpendicular ($\alpha$) or parallel ($\pi$) to the optical axis. (c) Luminescence spectra along the three polarization states. (d) Polar diagrams of the intensity ratio of 656 nm peak to 664 nm peak as a function of the polarization angle. Left diagram corresponds to front configuration while the diagram on the right is that for the side configuration.

When a nonspherical particle is optically trapped, stable position and orientation within the optical trap is achieved when the total optical forces and torques simultaneously vanish. Any slight displacement or rotation from this stable position (produced by, for instance, thermal energy) will be compensated by the appearance of a restoring force and torque that will return the particle to its stable state. While force equilibrium determines the stable position within the trap, torque equilibrium would determine the orientation of the trapped particle within the optical trap.[23] The appearance of optical torques (OTQs) during OT of nonspherical particles by single Gaussian laser beams has a complex origin. Particles of the order or smaller than the trapping wavelength are governed by the particle polarizability ($\alpha$) and thus by the laser-induced polarization ($\vec{P}_P$).[1,24] Former studies state that OTQs appear when $\vec{P}_P$ is not parallel to the trapping electrical field ($\vec{E}$) and stable orientation would be achieved when $\vec{P}_P$ and $\vec{E}$ are parallel (i.e., when OTQ vanishes). Previous works have identified two main mechanisms that could lead to the appearance of nonparallel $\vec{P}_P$ and $\vec{E}$ vectors.[25,26] The first one takes place when the optically trapped particle has a birefringent character.[27,28] In this case, when the light electric field is not parallel to any of the optical axes, the polarization vector $\vec{P}_P$ is not parallel to $\vec{E}$ due to the different polarizabilities along the different axes. Nonparallel $\vec{P}_P$ and $\vec{E}$ vectors could also occur if the optically trapped particle has a nonspherical shape.[24,29−31] In this case, the "effective" polarization becomes nonisotropic, leading to the appearance of a $\vec{P}_P$ vector whose orientation would be strongly dependent on the relative orientation between $\vec{E}$ and the "geometrical axis" of the particle. The presence of OTQs with different origins makes it difficult to predict the orientation of nonspherical particles inside optical traps. Indeed, full understanding on the OTQs appearing within optical traps requires the combination of experiments (observations of the stable orientation of the trapped particle) and numerical calculations (to determine the dominant mechanism causing this orientation). In this sense, nonspherical UCPs are excellent probes. As mentioned before, they show a highly polarized emission that allows for straightforward determination of their orientation when optically trapped by single particle polarized spectroscopy.[22] Despite its applied and fundamental interest, full description, modeling, and explanation of OTQs exerted on optically trapped nonspherical UCPs have not yet been explored.

In this work, the OTQs exerted on nonspherical UCPs inside a single beam optical trap have been experimentally studied. Their radial and axial stable orientation has been unequivocally determined by real time single particle polarized spectroscopy. The stable orientation states have been used to identify the different OTQs acting on the UCP. Furthermore, the physical mechanisms leading to the appearance of OTQs have been identified from the comparison between experimental data and numerical simulations. Finally, the rotation dynamics of optically trapped UCPs in different viscous media and inside living cells have been experimentally investigated. This has been applied for intracellular microrheology by using both a passive and an active method that leads to the estimation of the static and a dynamic cytoplasmic viscosity, respectively.

$\beta$-$NaYF_4$:$Er^{3+}$,$Yb^{3+}$ UCPs were synthesized by a hydrothermal processing as it is explained in the Supporting Information. Then, UCPs were suspended in distilled water for optical OT. As shown in Figure 1a, they have a hexagonal shape with a mean diameter and thickness of 800 and 400 nm, respectively. The $\beta$-$NaYF_4$:$Er^{3+}$,$Yb^{3+}$ UCPs used all along this


DOI: 10.1021/acs.nanolett.6b04583
Nano Lett. 2016, 16, 8005−8014

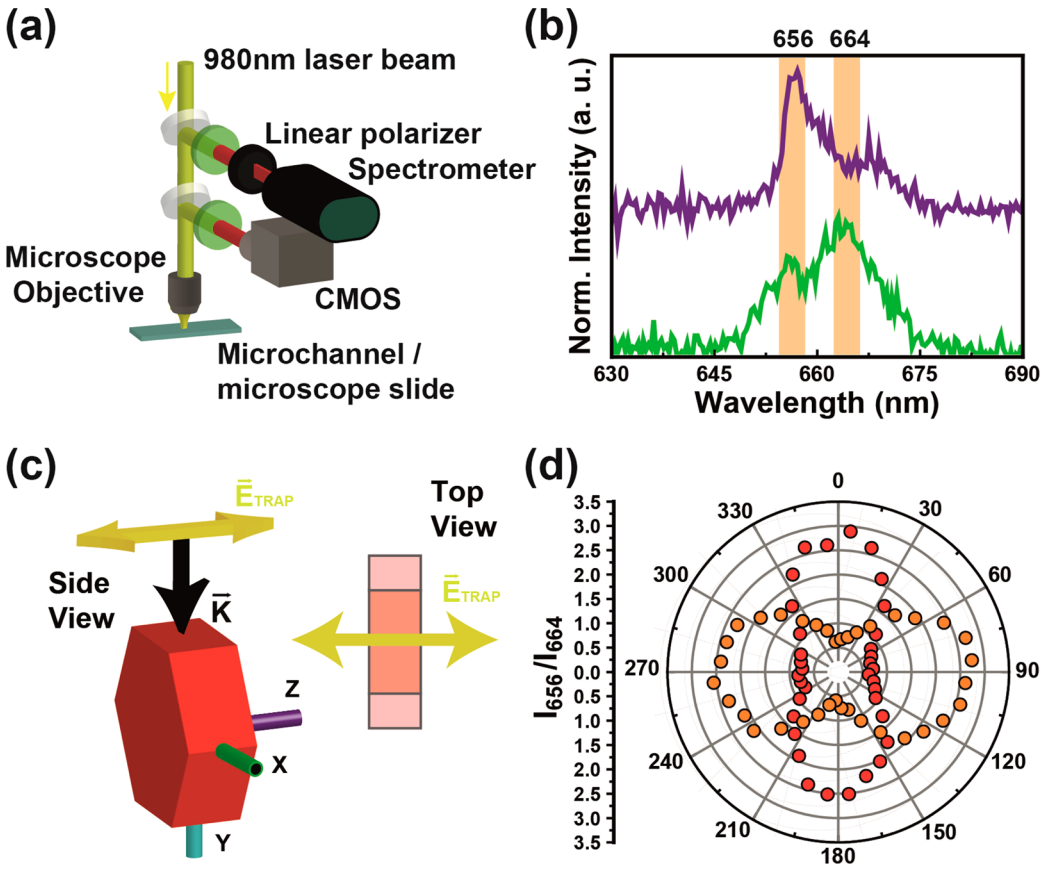


**Figure 2.** (a) Schematic representation of the experimental setup used for both luminescence characterization and optical trapping experiments. (b) Characteristic emission spectra obtained when a single UCP is incorporated to the optical trap obtained for a polarization parallel (purple) and perpendicular (green) to the linear polarization of the 980 nm trapping laser. (c) Diagram of the orientation of the trapped UCP in respect to the linear polarization of the trapping beam. (d) Polar diagrams of the ratio of 656 nm peak to 664 nm peak as a function of the polarization angle obtained for two perpendicular trapping laser polarizations.

work showed a strong green−red luminescence when optically excited with a 980 nm laser radiation via a two-photon excited process.[32−35] The different energy levels and physical mechanisms involved in this infrared excited visible luminescence are described in detail in the Supporting Information.[36]

The experimental setup used for simultaneous OT and single particle spectroscopy consists of a modified confocal microscope that integrates an optical trapping beam. A 980 nm linear polarized laser beam generated by a single mode fiber coupled diode is focused onto the sample by using a single microscope objective (0.85 NA). For the static characterization of the polarized emission of the UCPs, a diluted suspension ($2.3 \times 10^7$ UCPs/cm$^3$) of UCPs was dried over a microscope slide. The laser beam was then focused onto a single UCP. The single particle upconverting luminescence is collected by the same objective and after passing through several filters and apertures it is spectrally analyzed with a high sensitivity Si charge-coupled device camera (Synapse, Horiba) attached to a monochromator (iH320, Horiba). A linear polarizer (Thorlabs, LPNIR050-MP2) was placed at the entrance of the monochromator by using a rotating mount.

For OT and dynamical determination of single particle orientation, a diluted ($2.3 \times 10^7$ UCPs/cm$^3$) suspension of UCPs was injected into a 100 $\mu$m high microchannel (Ibidi Inc., $\mu$-Slide I 80106). For high viscosity transition time experiments, a mixture of water suspension of UCPs and Triton X-100 (Fluka) was prepared. Five hundred microliters of UCPs water suspension were added to 400 mg of Triton X-100. Then, the mixture was sonicated for more than 15 min and allowed to dry overnight. The resultant mixture had the consistence of a gel (more viscous than Triton X-100 on its own) with the UCPs distributed inside. For the experiments, the gel was spread over a microscope slide and covered by a coverslip. Transition time experiments were also performed inside HeLa cancer cells. The cells were incubated with a diluted ($1.1 \times 10^6$ UCPs/cm$^3$) solution of UCPs in phosphate saline buffer (PBS) for 2 h at 37 °C. More information can be found in the Supporting Information. During the incubation, the HeLa cells incorporated the UCPs by an endocytosis process. The cells were washed to eliminate possible UCPs remaining in the culture medium. For real time observation of UCP rotation (active method) and intensity ratio fluctuations (passive method), consecutive luminescence spectra were acquired with a maximum time resolution of 200 ms.

The possible polarization of the two-photon excited luminescence of the UCPs was investigated by studying individual particles deposited on a substrate by droplet drying. Single particle spectroscopy was performed by using a confocal microscope equipped with a 980 nm continuous wave laser diode that was focused by a 0.85 NA objective. When our UCPs are dried on a substrate, they orientated randomly with their largest facets either parallel (front configuration) or perpendicular (side configuration) to the substrate. Excitation was always perpendicular to the substrate. For this experiment,


DOI: 10.1021/acs.nanolett.6b04583
Nano Lett. 2016, 16, 8005−8014

we define the $z$-axis as that perpendicular to the hexagonal surface of our UCPs, and both $x$- and $y$-axes to be contained in the hexagonal surface (see schematic diagrams in Figure 1b). Our confocal microscope allows for characterizing the spectral shape of the emission for polarization states parallel to any of these three axes. The polarization angle was selected by rotating a linear polarizer placed at the entrance of the monochromator. Figure 1b shows the three main excitation configurations corresponding to the three main polarization states ($\sigma$, $\alpha$, $\pi$). $\sigma$-polarization state is defined for the light propagating along the optical axis ($z$-axis) with a polarization perpendicular to it (parallel to $x$- or $y$-axes). In $\alpha$- and $\pi$-polarization states, light propagates perpendicular to the optical axis of the UCP with a polarization parallel ($\pi$) or perpendicular ($\alpha$) to it. In this work, we have focused our attention on the red emission band of Erbium ions (corresponding to the $^4F_{9/2} \rightarrow {}^4I_{15/2}$ transition), because this particular transition is highly polarized in nonspherical UCPs.[21,22] The mechanism causing this highly polarization-dependent luminescence is not completely clear at this point but based on previous studies we state that this phenomenon is related to the crystalline structure of $NaYF_4$ lattice. $NaYF_4$ crystal lattice is uniaxial so that an optical axis does exist and the crystalline field is therefore expected to be nonisotropic. In this situation, the transition probabilities between Stark levels of Erbium ions become strongly dependent on the polarization of the emitted photon (for more information see Supporting Information). When the studied UCP is in front configuration, only $\sigma$-polarization could be studied. On the other hand, when the UCP is in side configuration, both $\alpha$- and $\pi$-polarizations are accessible. Polarized emission spectrum for each polarization is included in Figure 1c. This figure evidence that the polarization states parallel to either $x$- or $y$-axes are equivalent ($\sigma$- and $\alpha$-polarization states are equivalent), being different from the $\pi$-polarization state. This unequivocally reveals $\beta$-$NaYF_4$ UCPs as an uniaxial crystals. The most noticeable difference between $\sigma$- or $\alpha$- and $\pi$-spectra is the remarkable change in the intensity ratio between the emitted intensity at 656 and 664 nm ($I_{656}/I_{664}$). This is further evidenced in the polar plots included in Figure 1d corresponding to the polar variation of $I_{656}/I_{664}$ when collecting the luminescence along (left, front configuration) and perpendicularly (right, side configuration) to the optical axis. Insets show the relative orientation of the UCP in respect to the polar diagram. Polar diagrams were built by measuring the emission spectra for different orientations of the polarizer (different polarization angles) and then calculating for each case the intensity ratio of 656 nm peak to 664 nm peak. This polar plots reveals that luminescence collected along the optical axis is nonpolarized at all, with $I_{656}/I_{664} \approx 1$. On the other hand, when collecting the luminescence perpendicularly to the optical axis, the polar diagram evidences the presence of two polarization states, that is, those previously identified as $\alpha$- and $\pi$-states with $I_{656}/I_{664}$ values close to 1 and 3, respectively.

The strong polarization degree of the two-photon excited emission of our UCPs allows for a straightforward determination of their orientation when optically trapped by simultaneous OT and polarized spectroscopy. This can be simply achieved by coupling a single beam optical tweezer to a confocal microscope (see the schematic diagram in Figure 2a). A linearly polarized 980 nm laser beam was used to create the optical trap by focusing it into a microfluidic chamber by using a single 100× 0.85 NA microscope objective. A dilute suspension of UCPs was injected into the microchannel. Because 980 nm radiation is absorbed by the UCPs (see Supporting Information), their luminescence is an indicator of their incorporation to the optical trap. The two-photon excited visible luminescence of the trapped UCP was collected by the same microscope objective and spectrally analyzed with a high-resolution spectrometer equipped with a linear polarizer. Figure 2b shows two characteristic emission spectra obtained when a single UCP is incorporated to the optical trap obtained for two orthogonal polarizations (parallel (purple) and perpendicular (green) to the linear polarization of the 980 nm trapping laser). According to Figure 1, we can identify these two spectra to those corresponding to $\alpha$- (green) and $\pi$- (purple) polarization states. This unequivocally concludes that when optically trapped the UCP aligns with their hexagonal surfaces parallel (optical axis perpendicular) to the $\vec{k}$ vector of the trapping laser beam as it is schematically represented in Figure 2c. This conclusion was found to be independent of the orientation of the polarization state of the 980 nm trapping beam. The stability of the particle orientation inside the trap was checked by applying a perturbation (displacing 980 nm spot) along the radial and axial directions. It was observed that the trapped UCP keeps its orientation after any perturbation, because no change in the luminescence spectrum was observed. This preliminary analysis provides evidence that the particle is trapped in side configuration. Furthermore, the $\pi$-polarization state corresponds to the light being polarized along the optical axis of the particle (purple spectrum in Figure 2b). This spectrum also corresponds to a polarization parallel to the laser polarization, so that we can conclude that the particle orientates with its optical axis parallel to the laser polarization. This result is schematically represented in Figure 2c. In order to corroborate this fact and get a further insight into the role played by the 980 nm laser polarization on UCP orientation, the polarized emission spectrum as a function of the polarization angle was measured for two arbitrary orthogonal polarizations of the 980 nm laser beam. Results are summarized in the polar diagrams included in Figure 2d. A 90° rotation of the polar diagrams was found when the polarization of the trapping beam was rotated by 90°. A detailed analysis of these polar diagrams concluded that the UCP, once trapped in the side configuration, rotates around either its $x$- or $y$-axis until its $z$-axis (optical axis) is parallel to the $\vec{E}$ vector. Results included in Figure 2 evidence the existence of two different torques acting on the optically trapped UCPs:

(i) Axial OTQ. This induces a rotation of the particle around an axis perpendicular to the $\vec{k}$ vector of the trapping beam until the stable position (side configuration) is achieved for $\theta = 90°$, being $\theta$ the angle between $\vec{k}$ vector and the optical axis of the UCP.

(ii) Radial OTQ. This second torque induces a rotation of the UCP around its $x$- or $y$-axis until a stable position is achieved for $\varphi = 90°$ where in this case $\varphi$ is defined as the angle between the perpendicular direction to the optical axis of the UCP and the electric field vector of the laser trapping beam ($\vec{E}$).

Experimental data clearly evidence the existence of axial and radial OTQs but without providing much information about the underlying physical mechanisms. In order to get a deeper understanding on these OTQs, numerical simulations of the electromagnetic interaction between the electromagnetic field and the single trapped UCP have been conducted based on the finite element method.[37] In particular, a nonbirefringent hexagonal particle (800 nm in diameter and 400 nm thick)


DOI: 10.1021/acs.nanolett.6b04583
Nano Lett. 2016, 16, 8005−8014

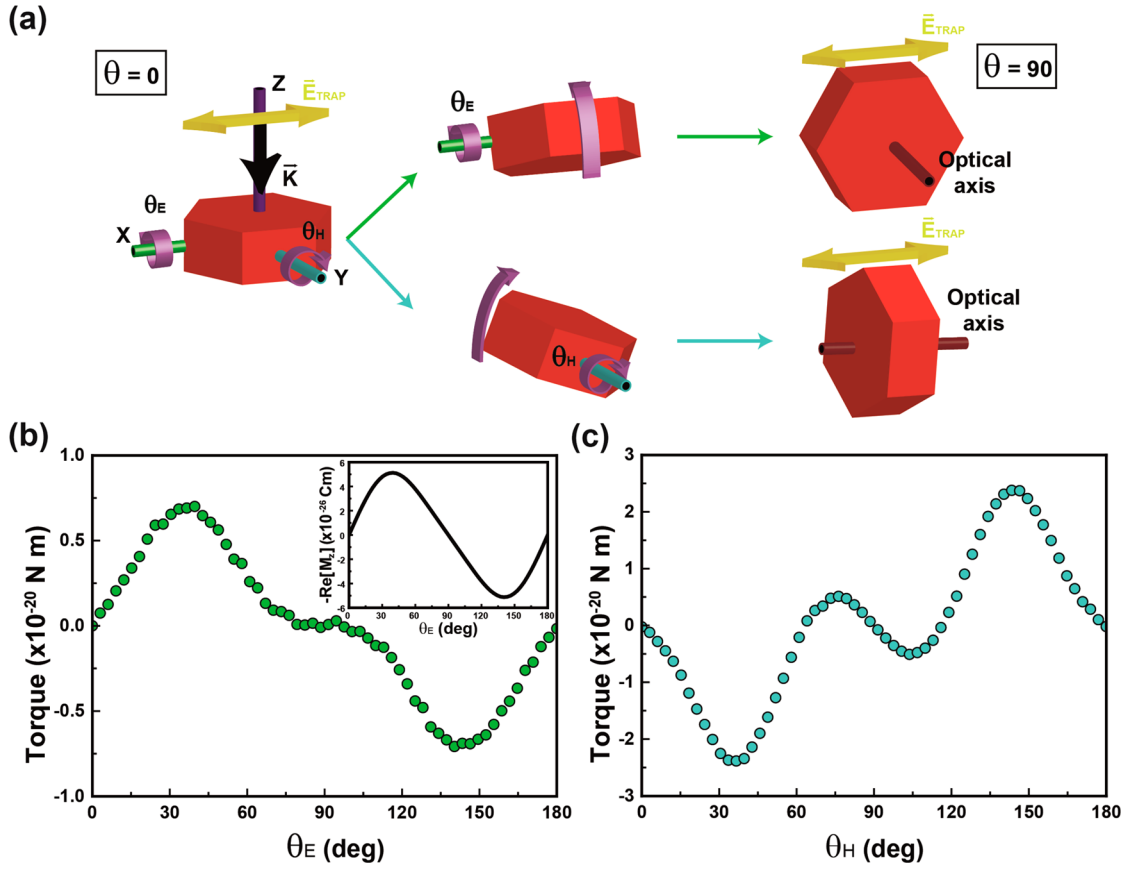


**Figure 3.** (a) Schematic representation of the two possible rotations associated with the transition from front to side configuration. Green path correspond to rotation around *x*-axis, while blue path illustrates rotation around *y*-axis. (b) Numerical torque calculated for a rotation around the *x*-axis. Inset: Minus the real part of the magnetic dipole as a function of the rotation angle. (c) Numerical torque calculated for a rotation around the *y*-axis.

illuminated by a linearly polarized 980 nm plane wave has been considered. The OTQ, $\langle\vec{\Gamma}\rangle$, acting on the UCP is calculated by integrating the Maxwell stress tensor $\boldsymbol{T}$ over an arbitrary surface $S$ enclosing the particle.[38] The components of the Maxwell Stress tensor are given by

$$T_{ij} = \left[\epsilon_0\epsilon E_i E_j + \mu_0 H_i H_j - \frac{1}{2}(\epsilon\epsilon_0 E^2 + \mu_0 H^2)\delta_{ij}\right] \quad (1)$$

where $\epsilon_0$ and $\epsilon$ are the vacuum and relative permittivity of the medium respectively, $\mu_0$ is the magnetic permeability, $E_i$ and $H_i$ are the $i$ component of electric and magnetic fields in the integration surface, $E$ and $H$ are the absolute value of the electric and magnetic fields, and $\delta_{ij}$ is the Kronecker's delta. Once the Maxwell Stress tensor is calculated, the OTQs acting on the particle are obtained by computing

$$\langle\vec{\Gamma}\rangle = -\langle\oint_S \hat{n}(\mathbf{T}\times\vec{r})\mathrm{d}\vec{S}\rangle \quad (2)$$

with $\hat{n}$ as the normal vector to the integration surface.

We have first considered a UCP that is free to rotate around an axis perpendicular to the $\vec{k}$ vector of trapping light and parallel to either the now fixed *x*- or *y*-axis of the UCP. In this case, the rotation axis can be parallel or perpendicular to the electric field $\vec{E}$ (i.e., perpendicular or parallel to the magnetic field $\vec{H}$). These two cases are schematically represented in Figure 3a where the rotation angles determining the particle orientation in each case ($\theta_E$ and $\theta_H$) are indicated. It is important to notice that each rotation leads to a different final orientation between the optical axis of the UCP and $\vec{E}$ vector. The simulated angular dependence of the axial OTQ appearing in each case is shown in Figure 3b,c, respectively. A stable equilibrium configuration is obtained when the OTQ is null and its derivative with respect to the rotation angle is negative. In both cases ($\theta_E$ and $\theta_H$ rotations), this situation is found when $\theta_E$ or $\theta_H$ are equal to 90°. However, a stable configuration is also found at $\theta_H$ = 0, implying that rotation to 90° must be performed around the axis parallel to $\vec{E}$ vector (around *x*-axis). This indicates that the UCP reaches a stable preliminary position when its optical axis is perpendicular to the propagation direction of trapping beam (i.e., UCP is in side configuration). This is in full agreement with the single particle polarized spectroscopy results (see Figure 2).

In order to better understand the physical mechanisms behind this rotation, we have numerically calculated the electric $\vec{P}$ and magnetic $\vec{M}$ dipole contributions of the particle. These are given by[39]

$$\vec{P} = \frac{i}{\omega}\int d^3r\vec{J} \quad (3)$$

$$\vec{M} = \frac{1}{2c}\int d^3r(\vec{r}\times\vec{J}) \quad (4)$$

with the displacement current $\vec{J}$ being related to the electric field inside the particle by

$$\vec{J} = -i\omega\epsilon_0(\epsilon - 1)\vec{E} \quad (5)$$



DOI: 10.1021/acs.nanolett.6b04583
*Nano Lett.* 2016, 16, 8005−8014

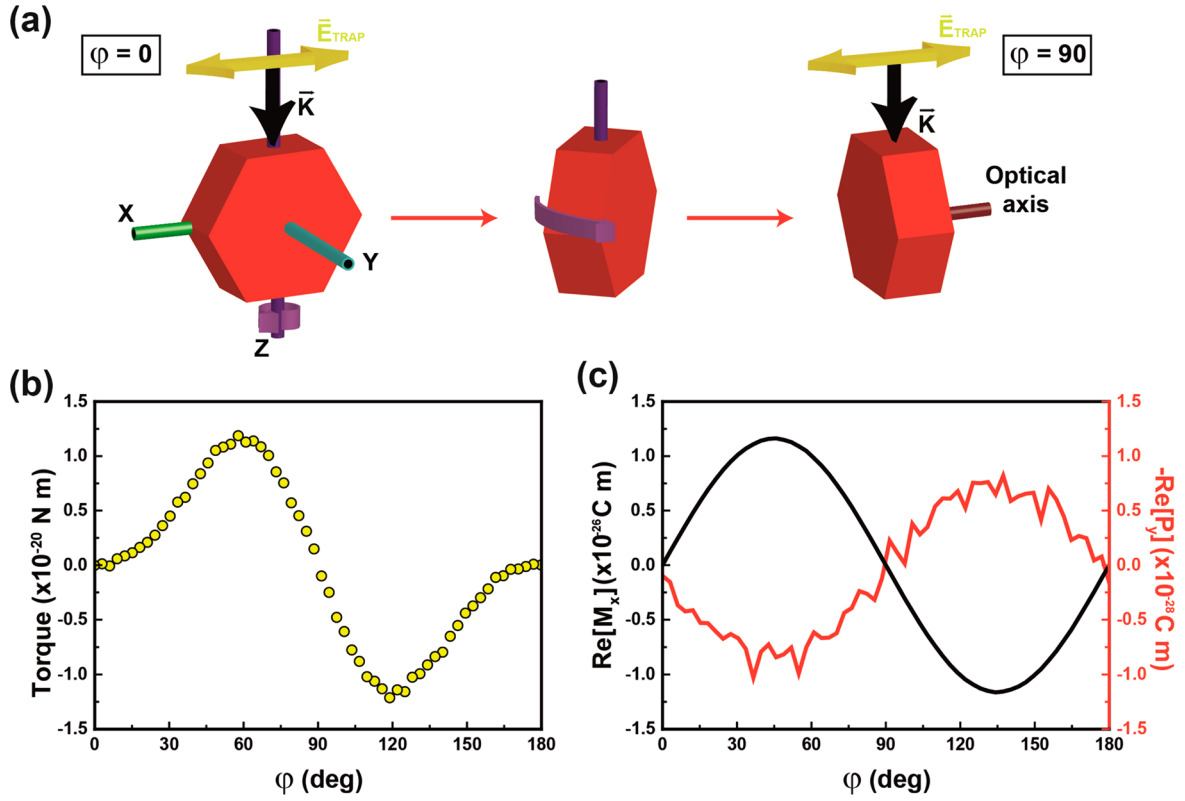


**Figure 4.** (a) Schematic representation of the rotation around $z$-axis. (b) Numerical torque calculated for a rotation around the $z$-axis considering the system depicted in (a). (c) Real part of the numerical magnetic and electric dipoles as a function of the rotation angle.

For the particular situation of an electromagnetic response mainly described by an electric and a magnetic dipole, the OTQ under linearly polarized plane wave illumination is given by[40]

$$\vec{\Gamma} = \frac{1}{2}\mathcal{R}[(\vec{P} \times \vec{E}^*) + (\vec{M} \times c\vec{B}^*)] \tag{6}$$

For the geometric configuration considered, where $\vec{E}$ is oriented in the $x$-direction and the wave propagates in the $z$-axis (see Figure 3a), the only contribution to the OTQ comes from the $z$-component of the magnetic dipole

$$\vec{\Gamma} = -\frac{1}{2}\mathcal{R}(M_z cB^*)\hat{u}_x \tag{7}$$

In the inset of Figure 3b, the angular dependence of the minus real part of the $z$-component of the magnetic dipole is shown. As OTQ is proportional to the minus real part of the $z$-component of the magnetic dipole (see expression 7), inset in Figure 3b predicts a stable configuration at 90°. This is in good agreement with both experimental data and numerical simulations, indicating the dominant role played by magnetic dipole interactions in the rotation and alignment of UCPs in an optical trap.

Once the particle is in side configuration, we have calculated the radial OTQ for a rotation around the $z$-axis. Results are shown in Figure 4. In this case, rotation is described in terms of the $\varphi$-angle, defined as the angle between the direction perpendicular to the optical axis and the $\vec{E}$ vector. The numerically simulated (using expression 2) angular dependence of the radial OTQ is shown in Figure 4b. A stable configuration is obtained for $\varphi = 90°$, that is, UCP rotates until its optical axis aligns with $\vec{E}$, which is in full agreement with experimental data (see Figure 2c).

As before, we have calculated the electric and magnetic dipoles of the particle for different orientations using expressions 3 and 4. For the considered configuration (see Figure 4), the OTQ depends on the $x$-component of the magnetic dipole and $y$-component of the electric dipole

$$\vec{\Gamma} = \frac{1}{2}\mathcal{R}(M_x cB^* - P_y E^*)\hat{u}_z \tag{8}$$

In Figure 4c, we show the angular dependence of the real part of the dipole's (magnetic and electric) components. The dominant term is the magnetic dipole, which is 2 orders of magnitude larger than the electric term. This magnetic component is responsible for the equilibrium configuration found at $\varphi = 90°$. It is, therefore, concluded that magnetic dipole interactions between the trapping beam and the UCPs are responsible for the achievement of a stable orientation through axial and radial orientations.

Once OTQs acting over nonspherical UCPs have been experimentally described and their origin determined, it is now possible to extract additional knowledge for the rotation dynamics undergone by an optically trapped UCP. In particular, important information can be extracted from the transition time ($\Delta t_R$) required by the UCP to reach its stable orientation. This would depend on the dynamic viscosity ($\eta$) of the medium in which the particle is suspended. As it is described in the Supporting Information, in a first order approximation the transition time can be written as

$$\Delta t_R = \beta \int_{\theta_i}^{\theta_f} \frac{1}{\langle \vec{\Gamma} \rangle} \, d\theta \tag{9}$$



DOI: 10.1021/acs.nanolett.6b04583
Nano Lett. 2016, 16, 8005−8014

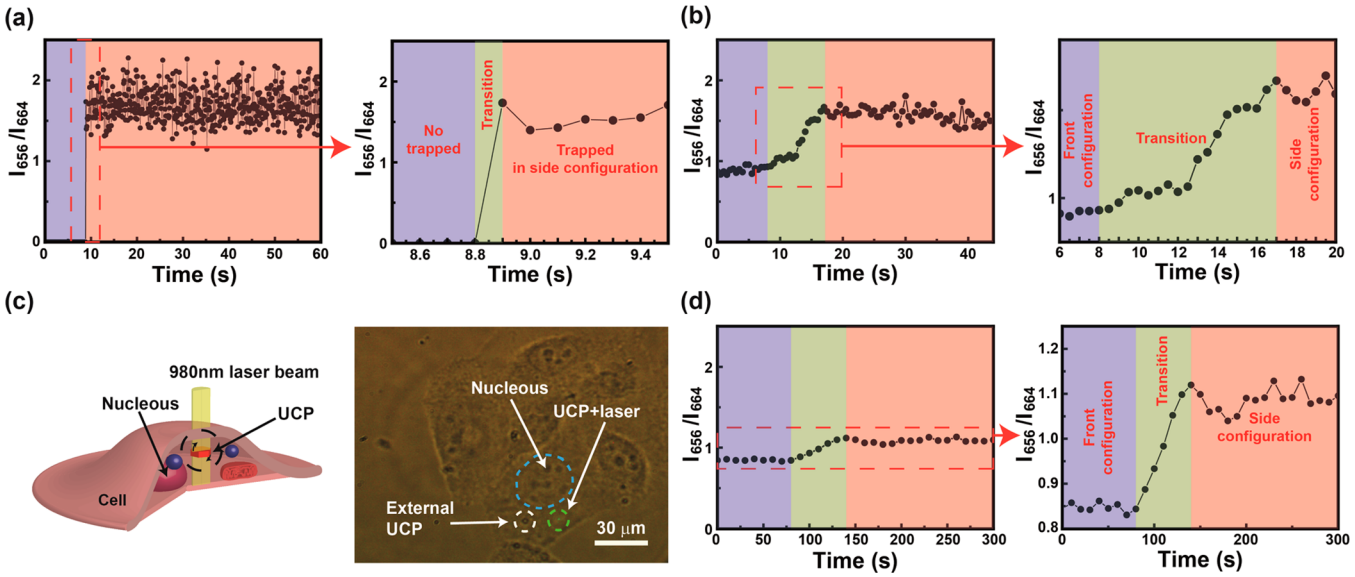


**Figure 5.** Evolution with time of the intensity ratio ($I_{656}/I_{664}$) for a rotation of a UCP immersed in water (a) and in a Triton X-100 based mixture (b). In (a), a null value of the ratio represents that the particle is not trapped. (c) Schematic representation (left) of the rotation of a UCP inside a HeLa cell (optical image on the right). (d) Evolution with time of the rotation of a UCP inside a HeLa cancer cell.

where $\beta$ is the rotational viscous friction factor of the particle in the medium and $\langle\vec{\Gamma}\rangle$ is the OTQ calculated by using expression 2. In expression 9, $\theta_i$ and $\theta_f$ are the initial and final orientation angles. For a complete transition, we can consider that the UCP incorporates into the trap with its optical axis parallel to the $\vec{k}$ vector of the trapping beam (front configuration) in such a way that $\theta_i = 0$. The final orientation is achieved when optical axis is perpendicular to the $\vec{k}$ vector of trapping beam (side configuration) in such a way that $\theta_f = 90°$. As it is explained in detail in the Supporting Information, the rotational viscous friction factor is proportional to $\eta$ in such a way that this final orientation can be obtained from the experimental determination of the transition time for a given applied laser power density ($I_L$)

$$\eta \approx 6.7 \times 10^{-14} \Delta t_R I_L \tag{10}$$

Figure 5 shows the time evolution of the intensity ratio $I_{656}/I_{664}$ of a UCP when optically trapped in three different media. When suspended in water (Figure 5a) the intensity ratio $I_{656}/I_{664}$ has a time-independent value close to 2, indicating that once the UCP enters into the trap it undergoes a fast rotation to its stable orientation. In this case, no transient/intermediate orientations are observed. This suggest that transition time is well below our time resolution (200 ms), so that $\Delta t_R(H_2O) <$ 0.2 s. Indeed, taking into account the dynamic viscosity of water (0.8 mPa s), expression 10 predicts (for a laser power density of $6.4 \times 10^{10}$ W/m$^2$) a rotation time close to $\Delta t_R(H_2O) \approx 190$ ms, so that it is not detectable in our experimental conditions. Data included in Figure 5b correspond to the time evolution of the intensity ratio as obtained from an optically trapped UCP suspended in a Triton X-100 based mixture that has been prepared following the procedure described above. In this case, due to the large viscosity of the mixture a clear orientation transition was observed. From data included in Figure 5b, a transition time of $\Delta t_R$(Triton) = 9.0 ± 0.6 s was measured for a laser power density of $2.4 \times 10^{11}$ W/m$^2$. As shown in Figure S5 of Supporting Information, the rotation time of an optically trapped UCP in the Triton X-100 based mixture was found to increases linearly with the inverse of the trapping laser power density (i.e., $\Delta t_R \propto 1/I_L$), being this in agreement with expression 10. As it is also described in detail in the Supporting Information, the analysis of the transition times provides a dynamic viscosity for the mixture of $\eta$(Triton) = 210 ± 30 mPa·s, that it is very close to that experimentally determined by using a vibro viscometer (170 ± 1 mPa·s). The agreement found between these two different approaches validates the use of the transition time of optically trapped UCP for the determination of medium dynamic viscosity.

The analysis of rotation dynamics of a single UCP was finally used for the remote determination of the intracellular dynamic viscosity. As it is described in detail in the Supporting Information, HeLa cancer cells were incubated with a suspension containing UCPs in such a way that, as a results of an endocytosis process, some of the UCPs were incorporated into the cells (see schematic representation and optical image in Figure 5c). We performed up to 34 different measurements over more than 20 different HeLa cells (see some representative optical images in Figure S1). Intracellular viscosity was determined by two methods. The first method, hereafter denoted as "active" method, is the same procedure used for the determination of the viscosity of water and the Triton X-100 based mixture. It is based on the time required by the UCP to perform a complete 90° rotation as forced by the optical torque. Because intracellular viscosity is known to be frequency dependent (i.e., it depends on the deformation rate),[41] expression 10 has been rewritten as

$$\eta = \frac{\pi}{2} \frac{6.7 \times 10^{-14}}{\omega_R} I_L \tag{11}$$

where $\omega_R$ is the rotation frequency of the UCP and thus the frequency at which intracellular viscosity is evaluated. In a first order approximation, this rotation frequency can be directly estimated from the time required for a 90° rotation: $\omega_R = 2\pi/\Delta t_R$.

Figure 5d shows, as a representative example, the time evolution of the intensity ratio $I_{656}/I_{664}$ as obtained for an intracellular UCP optically trapped with a power density of 4.1



DOI: 10.1021/acs.nanolett.6b04583
Nano Lett. 2016, 16, 8005−8014

**Table 1. Measured Viscosity Values for Both Active and Passive Method**[a]

| exp. | area inside cell | method | mean rotation frequency (rad/s) | laser power intensity ($\times 10^{10}$W/m$^2$) | viscosity (Pa s) |
|---|---|---|---|---|---|
| 1 | DM | passive | | 1.2 ± 0.2 | 2.13 ± 0.02 |
| 2 | SCNM | passive | | 1.3 ± 0.2 | 2.90 ± 0.03 |
| 3 | SCNM | passive | | 1.3 ± 0.2 | 1.95 ± 0.02 |
| 4 | FM | passive | | 2.7 ± 0.2 | 2.06 ± 0.06 |
| 5 | SCNM | passive | | 2.7 ± 0.2 | 2.71 ± 0.03 |
| 6 | no record | passive | | 3.7 ± 0.2 | 1.65 ± 0.04 |
| 7 | CPNM | passive | | 4.1 ± 0.2 | 1.98 ± 0.02 |
| 8 | CPNM | passive | | 4.1 ± 0.2 | 2.44 ± 0.02 |
| 9 | SCNM | passive | | 4.1 ± 0.2 | 2.80 ± 0.02 |
| 10 | FM | passive | | 5.9 ± 0.2 | 2.17 ± 0.03 |
| 11 | FM | active | 0.00196 ± 0.00001 | 2.7 ± 0.2 | 1.45 ± 0.09 |
| 12 | CPNM | active | 0.04223 ± 0.004 | 2.7 ± 0.2 | 0.07 ± 0.01 |
| 13 | ANM | active | 0.00255 ± 0.00001 | 2.7 ± 0.2 | 1.12 ± 0.07 |
| 14 | ANM | active | 0.00845 ± 0.0001 | 3.7 ± 0.2 | 0.46 ± 0.03 |
| 15 | FM | active | 0.02618 ± 0.0003 | 4.1 ± 0.2 | 0.17 ± 0.03 |
| 16 | SCNM | active | 0.00278 ± 0.00002 | 4.8 ± 0.2 | 1.80 ± 0.07 |

[a]DM, distant from any membranes; SCNM, slightly close to nuclear membrane; CPNM, in close proximity to nuclear membrane; ANM, At nuclear membrane. See Figure S1 for more information about the areas inside cell.

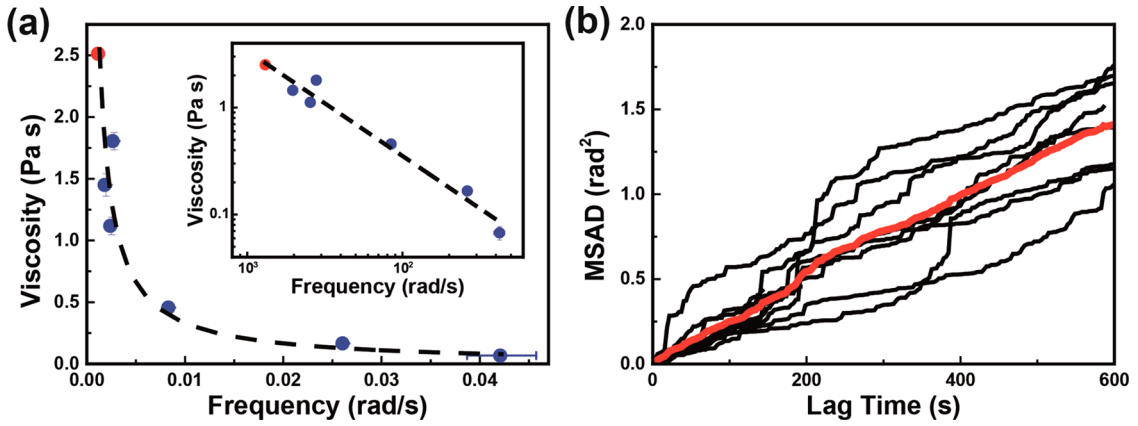


**Figure 6.** (a) Measured viscosity as a function of the rotation frequency. Inset is the log−log representation. Blue data correspond to the values measured by the active method while red data is the averaged value obtained from passive method experiments. The rotation frequency for passive method is estimated by dividing the accumulated rotated angle by the elapsed drag. Black dashed lines correspond to the best fitting. (b) MSAD as a function of the lag time for a total set of 10 particles. Red line correspond to the main trajectory.

x$10^{10}$ W/m$^2$ (exp. 15 in Table 1). Under these conditions, experimental data reveals a transition time of $\Delta t_R = 60 \pm 10$ s (or $\omega_R = 2.78 \times 10^{-3} \pm 0.02 \times 10^{-3}$ rad/s). This, according to expression 11, leads to an intracellular dynamic viscosity for this particular frequency of $\eta(2.78 \times 10^{-3}$ rad/s) = 170 ± 30 mPa·s. The same experimental and analytical procedure was performed over a total number of 16 different UCPs located in different HeLa cells and by using different laser trapping intensities, leading to different rotation frequencies. The obtained values of intracellular viscosity and their corresponding rotation frequencies are included in Table 1. These data have been also included in Figure 6a in which the reduction of intracellular viscosity with rotation frequency is evidenced as it was, indeed, expected.

Intracellular viscosity was also determined by a second approach hereafter refereed as "passive" method. It is based on the analysis of the mean square angular displacement (MSAD) as a function of the lag time. In particular, the angular displacement was obtained from the analysis of the time fluctuations of the fluorescence intensity ratio $I_{656}/I_{664}$ as it is explained in detail in Supporting Information. For these experiments only particles in side configuration were used to ensure that no complete rotation occurs during the measure. Figure 6b shows a set of MASDs as a function of the lag time ($\tau$) obtained for a total number of 10 particles. Black lines correspond to the individual trajectories whereas the red line corresponds to the averaged trajectory. For each trajectory, a value for the viscosity could be obtained[42−46]

$$\mathrm{MSAD(rad^2)} = \frac{RT}{3\eta V_p f / f_0}\tau^{\alpha} \tag{12}$$

where $\alpha$ determines whether the movement of the particle is restricted ($\alpha < 1$) or it experiences superdiffusion ($\alpha > 1$). In our case we set $\alpha$ to 1 since the angular displacement is assumed to only be due to Brownian motion. The result for each trajectory could be found in Table 1. The average trajectory gives a mean viscosity of 2.51 ± 0.01 Pa s. The obtained values have a certain dispersion attributed to the high sampling variability of HeLa cells, as reported in previous studies.[47] Even when all particles were enclosed by a vesicle due to internalization, they were located in different cells and areas inside them as it is shown in Figure S1.



DOI: 10.1021/acs.nanolett.6b04583
Nano Lett. 2016, 16, 8005−8014

Figure 6a includes the intracellular viscosity values obtained by both passive and active methods (red and blue dots, respectively) as a function of rotation frequency. In this graph, the red dot corresponds to the mean viscosity value obtained from all passive measurements. The rotation frequency in this case is estimated by dividing the accumulated rotated angle by the elapsed drag (1.18 rad in 600 s leading to an effective rotation frequency close to 0.002 rad/s). Inset in Figure 6a shows the linear dependence with a slope around −1 in a log−log representation. Figure 6a reveals that the viscosity in the cytoplasm has a mean static value of around 2.51 Pa s which decreases monotonously with increasing frequency. From the log−log representation we can conclude that $\eta \sim 1/\omega_R$. This fact points out that at this range of frequencies the cytoplasm behaves as a viscous liquid as demonstrated by former studies.[41,48]

Our experimental results included in Table 1 and Figure 6a can be now compared with those previously reported by authors also employing similar passive and active methods. In Table S1, we present the results obtained from different studies on the inner cell viscosity of HeLa cells and NIH/3T3 fibroblast. Table S1 indeed reflects the large dispersion of the values reported in the literature for the intracellular viscosity of HeLa cells. The results presented here, ranging from 2.90 down to 0.07 Pa·s, are comparable to the values found in literature for other probes of similar sizes. In any case, comparison of our experimental results with previously reported is not an easy task due to different factors. First, viscosity depends on the probe size.[41,43] Kalwarczyk et al. obtained that the viscosity increases as the probe size does, being constant (microscopic/mesoscopic viscosity) for particles larger than the effective mesh size (or mean radius of the cytoplasmic obstacles) of the cytoplasm.[43] In the case of HeLa Cells, Kalwarczyk et al. found that particles with hydrodynamic radii exceeding 350 nm would experience the macroscopic viscosity. Second, it has to be considered whether the particle is in direct contact with the cytoplasm or it is located inside a vesicle due to the phagocytosis process, as this is our case. Moreover, the particle could be coated by a substance that facilitates its transport inside the cytoplasm.[49] Therefore, apart from distinguising between active and passive methods, many other factors have to be consider when comparing the obtained results with those provided by the literature.

In summary, single particle polarized spectroscopy has been used to elucidate how an individual upconverting hexagonal particle orientates inside a single beam optical trap. It has been experimentally evidenced that a stable situation is achieved when the optical axis of the upconverting particle orientates parallel to the electric field vector of the infrared trapping radiation. Numerical simulations confirmed the existence of this stable configuration and provide an estimation of the magnitude of the dominant optical torques. Simple calculations concluded that the rotation of the studied upconverting particle inside the optical trap was mainly governed by dipole magnetic interactions.

Time-resolved single particle polarized spectroscopy experiments were designed and conducted to monitor in real time the rotation of individual upconverting particles once optically trapped. Analysis of real time experiments in combination with numerical calculations allowed for the determination of the dynamic viscosity of the medium in which the upconverting particle is suspended. This procedure was applied for the determination of the intracellular dynamic viscosity. Two methods were used leading to the estimation of the static (passive method) and dynamic viscosity (active method). It has been found that the dynamic viscosity decreases with the rotating frequency in the studied rage of frequencies. Moreover, the obtained values were found in reasonable agreement with previous studies. The relevant role played by the organic compounds encapsulating the upconverting particle in the cytoplasm is also discussed.

This work provide a new step toward the complete understanding over the light-matter interactions at the micro- and nanoscale. It also introduces real time single particle spectroscopy as the unique technique to study three-dimensional particle dynamics with great potential in numerous fields ranging for micro/nano fluidics to single cell studies.

## ■ ASSOCIATED CONTENT

### Supporting Information

The Supporting Information is available free of charge on the ACS Publications website at DOI: 10.1021/acs.nanolett.6b04583.

Experimental section, upconversion process, and transition time (PDF)

## ■ AUTHOR INFORMATION


### Corresponding Author

*E-mail: daniel.jaque@uam.es.


### Author Contributions

The manuscript was written through contributions of all authors. All authors have given approval to the final version of the manuscript.


### Funding

This work was supported by the Spanish Ministerio de Educación y Ciencia (MAT2013-47395-C4-1-R and MAT2016-75362-C3-1-R), by Banco Santander for "Proyectos de Cooperación Interuniversitaria" (2015/ASIA/06) and by COST Action 1403.


### Notes

The authors declare no competing financial interest.

## ■ ACKNOWLEDGMENTS


P.H.G. thanks the Spanish Ministerio de Economía y Competitividad (MINECO) for the Juan de la Cierva program. P.R.S. thanks MINECO and the Fondo Social Europeo (FSE) for the "Promoción del talento y su Empleabilidad en I+D+i" statal program (BES-2014-069410). M.I.M. acknowledges the financial support from MINECO Grant FIS2015-69295-C3-3-P and from the María de Maeztu Programme for Units of Excellence in R&D (Grant MDM-2014-0377). N.d.S. thanks MINECO for grants FIS2012-36113-C03, FIS2015-69295-C3-3-P, and MAT2014-58860-P and the Comunidad de Madrid (Contract No. S2013/MIT-2740). J. R. Procopio and M. T. Sevilla are acknowledged for material support. A. García-Martín is gratefully acknowledged for supporting computing facilities.


## ■ ABBREVIATIONS

3D, three-dimensional; OT, optical trapping; UCPs, upconverting particles; OTQs, optical torques

## ■ REFERENCES


(1) Neuman, K. C.; Block, S. M. *Rev. Sci. Instrum.* **2004**, *75* (9), 2787−2809.




DOI: 10.1021/acs.nanolett.6b04583
*Nano Lett.* 2016, 16, 8005−8014

(2) Svoboda, K.; Block, S. M. *Annu. Rev. Biophys. Biomol. Struct.* **1994**, *23*, 247−285.
(3) Nakayama, Y.; Pauzauskie, P. J.; Radenovic, A.; Onorato, R. M.; Saykally, R. J.; Liphardt, J.; Yang, P. *Nature* **2007**, *447* (7148), 1098−1101.
(4) Blehm, B. H.; Schroer, T. A.; Trybus, K. M.; Chemla, Y. R.; Selvin, P. R. *Proc. Natl. Acad. Sci. U. S. A.* **2013**, *110* (9), 3381−3386.
(5) Leidel, C.; Longoria, R. A.; Gutierrez, F. M.; Shubeita, G. T. *Biophys. J.* **2012**, *103* (3), 492−500.
(6) Oroszi, L.; Galajda, P.; Kirei, H.; Bottka, S.; Ormos, P. *Phys. Rev. Lett.* **2006**, *97* (5), 058301.
(7) Gu, M.; Bao, H. C.; Gan, X. S.; Stokes, N.; Wu, J. Z. *Light: Sci. Appl.* **2014**, *3*, e126.
(8) Johansen, P. L.; Fenaroli, F.; Evensen, L.; Griffiths, G.; Koster, G. *Nat. Commun.* **2016**, *7*, 10974.
(9) Ashkin, A.; Dziedzic, J. *Science* **1987**, *235* (4795), 1517−1520.
(10) Ashkin, A. *Proc. Natl. Acad. Sci. U. S. A.* **1997**, *94* (10), 4853−4860.
(11) Haro-Gonzalez, P.; del Rosal, B.; Maestro, L. M.; Martin Rodriguez, E.; Naccache, R.; Capobianco, J. A.; Dholakia, K.; Sole, J. G.; Jaque, D. *Nanoscale* **2013**, *5* (24), 12192−12199.
(12) Jauffred, L.; Oddershede, L. B. *Nano Lett.* **2010**, *10* (5), 1927−1930.
(13) Pelton, M.; Liu, M.; Kim, H. Y.; Smith, G.; Guyot-Sionnest, P.; Scherer, N. F. *Opt. Lett.* **2006**, *31* (13), 2075−2077.
(14) Selhuber-Unkel, C.; Zins, I.; Schubert, O.; Sonnichsen, C.; Oddershede, L. B. *Nano Lett.* **2008**, *8* (9), 2998−3003.
(15) Bendix, P. M.; Jauffred, L.; Norregaard, K.; Oddershede, L. B. *IEEE J. Sel. Top. Quantum Electron.* **2014**, *20* (3), 15−26.
(16) Rodríguez-Sevilla, P.; Rodríguez-Rodríguez, H.; Pedroni, M.; Speghini, A.; Bettinelli, M.; Solé, J. G.; Jaque, D.; Haro-González, P. *Nano Lett.* **2015**, *15* (8), 5068−5074.
(17) Mor, F. M.; Sienkiewicz, A.; Forró, L.; Jeney, S. *ACS Photonics* **2014**, *1* (12), 1251−1257.
(18) Fan, X.; Zheng, W.; Singh, D. J. *Light: Sci. Appl.* **2014**, *3*, e179.
(19) Xin, H.; Li, B. *Light: Sci. Appl.* **2014**, *3*, e205.
(20) Rodríguez-Sevilla, P.; Zhang, Y.; Haro-González, P.; Sanz-Rodríguez, F.; Jaque, F.; Solé, J. G.; Liu, X.; Jaque, D. *Adv. Mater.* **2016**, *28* (12), 2421−2426.
(21) Chen, P.; Song, M.; Wu, E.; Wu, B.; Zhou, J.; Zeng, H.; Liu, X.; Qiu, J. *Nanoscale* **2015**, *7* (15), 6462−6466.
(22) Rodriguez-Sevilla, P.; Labrador-Paez, L.; Wawrzynczyk, D.; Nyk, M.; Samoc, M.; Kar, A. K.; Mackenzie, M. D.; Paterson, L.; Jaque, D.; Haro-Gonzalez, P. *Nanoscale* **2016**, *8* (1), 300−308.
(23) Gauthier, R. C. *J. Opt. Soc. Am. B* **1997**, *14* (12), 3323−3333.
(24) Li, M.; Yan, S.; Yao, B.; Liang, Y.; Han, G.; Zhang, P. *J. Opt. Soc. Am. A* **2016**, *33* (7), 1341−1347.
(25) Nieminen, T. A.; Asavei, T.; Loke, V. L. Y.; Heckenberg, N. R.; Rubinsztein-Dunlop, H. *J. Quant. Spectrosc. Radiat. Transfer* **2009**, *110* (14−16), 1472−1482.
(26) Emile, O.; Emile, J. *Opt. Lett.* **2016**, *41* (2), 211−214.
(27) La Porta, A.; Wang, M. D. *Phys. Rev. Lett.* **2004**, *92* (19), 190801.
(28) Cheng, Z.; Chaikin, P. M.; Mason, T. G. *Phys. Rev. Lett.* **2002**, *89* (10), 108303.
(29) Bishop, A. I.; Nieminen, T. A.; Heckenberg, N. R.; Rubinsztein-Dunlop, H. *Phys. Rev. A: At., Mol., Opt. Phys.* **2003**, *68* (3), 033802.
(30) Xu, F.; Lock, J. A.; Gouesbet, G.; Tropea, C. *Phys. Rev. A: At., Mol., Opt. Phys.* **2008**, *78* (1), 013843.
(31) Borghese, F.; Denti, P.; Saija, R.; Iatì, M. A.; Maragò, O. M. *Phys. Rev. Lett.* **2008**, *100* (16), 163903.
(32) Wang, F.; Liu, X. *Chem. Soc. Rev.* **2009**, *38* (4), 976−989.
(33) Som, S.; Das, S.; Yang, C. Y.; Lu, C. H. *Opt. Lett.* **2016**, *41* (3), 464−467.
(34) Liu, N.; Shao, W.; Chen, G. *Science Advances Today* **2015**, *1*, 25211.
(35) Zhou, B.; Shi, B.; Jin, D.; Liu, X. *Nat. Nanotechnol.* **2015**, *10* (11), 924−936.
(36) Jung, T.; Jo, H. L.; Nam, S. H.; Yoo, B.; Cho, Y.; Kim, J.; Kim, H. M.; Hyeon, T.; Suh, Y. D.; Lee, H.; Lee, K. T. *Phys. Chem. Chem. Phys.* **2015**, *17* (20), 13201−13205.
(37) COMSOL. *Multiphysics*, version 5.2; http://www.comsol.com.
(38) Borghese, F.; Denti, P.; Saija, R.; Iatì, M. A. *Opt. Express* **2006**, *14* (20), 9508−9521.
(39) Radescu, E. E.; Vaman, G. *Phys. Rev. E: Stat. Phys., Plasmas, Fluids, Relat. Interdiscip. Top.* **2002**, *65* (4), 046609.
(40) Nieto-Vesperinas, M. *Opt. Lett.* **2015**, *40* (13), 3021−3024.
(41) Wirtz, D. *Annu. Rev. Biophys.* **2009**, *38* (1), 301−326.
(42) Chen, Y.-c.; Wu, C.-m. *Jpn. J. Appl. Phys.* **2012**, *51* (12R), 127001.
(43) Kalwarczyk, T.; Ziębacz, N.; Bielejewska, A.; Zaboklicka, E.; Koynov, K.; Szymański, J. d.; Wilk, A.; Patkowski, A.; Gapiński, J.; Butt, H.-J. r.; Hołyst, R. *Nano Lett.* **2011**, *11* (5), 2157−2163.
(44) Chevry, L.; Colin, R.; Abou, B.; Berret, J.-F. *Biomaterials* **2013**, *34* (27), 6299−6305.
(45) Lee, J. S. H.; Panorchan, P.; Hale, C. M.; Khatau, S. B.; Kole, T. P.; Tseng, Y.; Wirtz, D. *J. Cell Sci.* **2006**, *119* (9), 1760−1768.
(46) Yamada, S.; Wirtz, D.; Kuo, S. C. *Biophys. J.* **2000**, *78* (4), 1736−1747.
(47) Chen, S.; Hong, Y.; Zeng, Y.; Sun, Q.; Liu, Y.; Zhao, E.; Bai, G.; Qu, J.; Hao, J.; Tang, B. Z. *Chem. - Eur. J.* **2015**, *21* (11), 4315−4320.
(48) Berret, J. F. *Nat. Commun.* **2016**, *7*, 10134.
(49) Hui, Y. Y.; Zhang, B.; Chang, Y.-C.; Chang, C.-C.; Chang, H.-C.; Hsu, J.-H.; Chang, K.; Chang, F.-H. *Opt. Express* **2010**, *18* (6), 5896−5905.



DOI: 10.1021/acs.nanolett.6b04583
*Nano Lett.* 2016, 16, 8005−8014